* Corresponding author: Jiaxin Zhang

Email Address: jiaxinz@uow.edu.au

Secular Cooling Shapes Core-Mantle Heat Transfer and Mantle Plume Dynamics over 1.8 Billion Years

Authors: Jiaxin Zhang[1,*], Nicolas Flament[1], Stéphane Labrosse[2], Xianzhi Cao[3], Dietmar Müller[4], Annalise Cucchiaro[1]

[1] Environmental Futures, School of Science, the University of Wollongong, Wollongong, NSW 2522, Australia

[2] Laboratoire des sciences de la Terre, Ecole Normale Supérieure de Lyon, Université de Lyon, CNRS UMR 5570, 46 Allée d'Italie, 69364 Lyon Cedex 07, France

[3] Frontiers Science Center for Deep Ocean Multispheres and Earth System, Key Lab of Submarine Geosciences and Prospecting Techniques, MOE and College of Marine Geosciences, Ocean University of China, Qingdao 266100, China

[4] EarthByte Group, School of Geosciences, the University of Sydney, NSW 2006, Australia

Abstract

Petrological evidence and global heat budgets indicate that the solid Earth has cooled substantially over geological time, yet the influence of secular cooling on mantle dynamics in global 3D models remains poorly quantified. We incorporate secular cooling into 3D global mantle flow models using plate reconstructions extending back 1.8 billion years. The core-mantle boundary (CMB) temperature is modelled as decreasing over time in scenarios consistent with continuous outer-core dynamo action and inner-core crystallization. The internal heating rate is modelled as declining with radiogenic isotopes decay. By systematically varying convective vigour and core heat capacity, we demonstrate that secular cooling exerts a first-order control on deep mantle evolution. The CMB heat flux and the fractional area of Big LOwer-mantle Basal Structures (BLOBS) are strongly anti-correlated, highlighting slab–BLOBS interactions as central regulators of deep mantle heat transfer. Predicted plume heat flux broadly reproduces the long-term pattern of large igneous province eruptions. These results show that coupled core–mantle cooling is essential for reconstructing Earth's thermochemical evolution over billion-year timescales and to link plume dynamics with geological observables.

Keywords: mantle convection; secular cooling; core-mantle boundary; heat flow; mantle plume

Highlights

- We incorporate secular cooling in 3D global mantle flow models
- The models use a plate tectonic reconstruction extending back 1.8 billion years
- Secular cooling exerts a first-order control on global mantle dynamics
- The model-predicted plume flux broadly matches Large Igneous Province records

1. Introduction

Global heat budgets and petrological evidence indicate that the bulk silicate Earth has been cooling over the past hundreds of millions of years. Current surface heat loss is between 43–49 TW, of which between 15–25 TW is supplied by radiogenic heating. Diverse estimates based on requirements to maintain dynamo action in Earth's outer core, mantle plume heat flux, and the thermal gradient of perovskite to post-perovskite phase transition (e.g., Labrosse and Jaupart, 2007; Lay et al., 2008; Nakagawa, 2020) suggest that the heat flow across the core-mantle boundary (CMB) accounts for between 5–15 TW of Earth's secular cooling, leaving between 8–28 TW of heat loss which is the secular cooling of the mantle (Fig. 1), which corresponds to a present cooling rate between 60–210 K Gyr^{-1}. Petrological studies further suggest that the Archaean mantle was ~100–300ºC hotter than today (e.g., Abbott et al., 1994; Grove and Parman, 2004).

The secular cooling of the solid Earth is the imbalance between total heat loss and energy generated within the planet (e.g., Jaupart et al., 2015). Although uncertain, secular cooling accounts for ~40% of Earth's total energy budget (Korenaga, 2006) and influences the long-term evolution of heat in Earth's core and mantle (e.g., Nakagawa, 2020; Nimmo, 2015). Two important aspects of Earth's secular cooling are the decrease in CMB temperature and internal heating rate. The vigour of mantle convection is expected to have decreased with CMB temperature throughout Earth's history, and mantle potential temperature is expected to have decreased with internal heating rate (e.g., Li et al., 2023), cooling the mantle, and decreasing the effective Rayleigh number. Although the importance of secular cooling in mantle dynamics has long been recognized (e.g., Sharpe and Peltier, 1979; Nakagawa and Tackley, 2004; Li et al., 2023), self-consistent secular cooling has not been included in global 3D mantle convection models driven by plate tectonic reconstructions. As a result, the evolution of CMB heat flow which affects the area of BLOBS and the number of plumes trough time remain poorly-

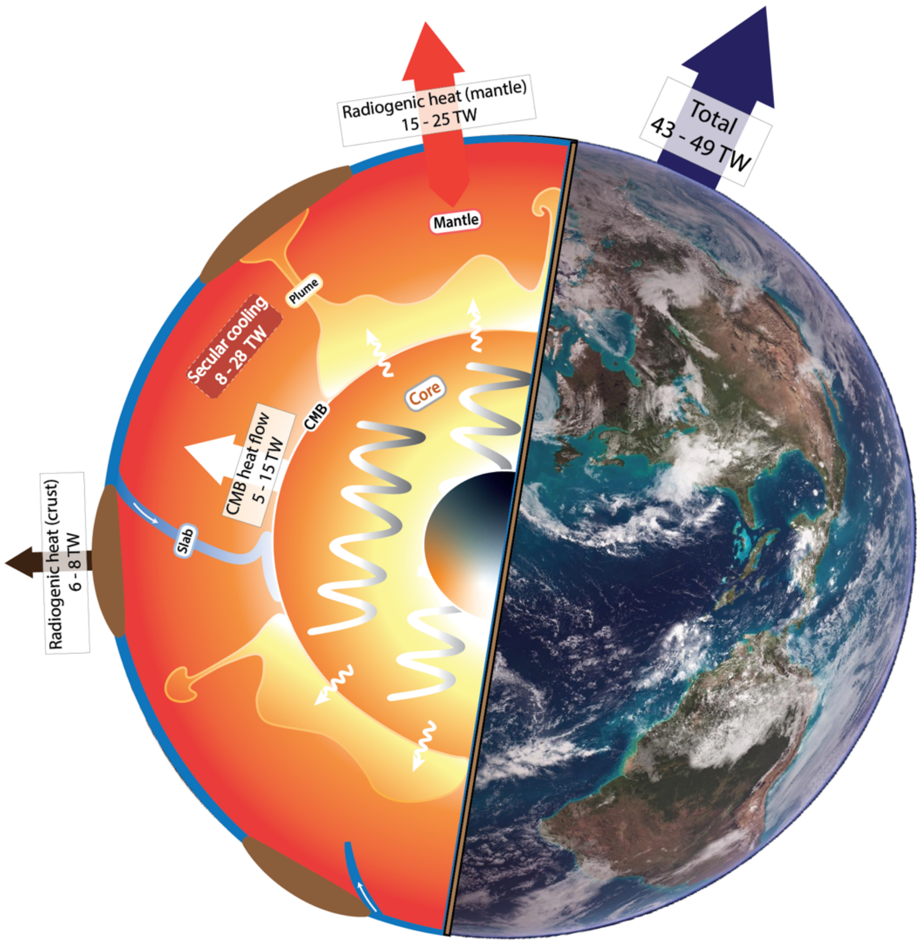

Figure 1. Schematic illustrating Earth's heat budget. The left semi-sphere shows the cross-section of the schematic dynamic processes in Earth's interior, including mantle and core convection. The global heat loss from the surface is approximately between 43–49 TW, with between 15–25 TW due to radiogenic heat production and between 8–28 TW due to present-day secular cooling, according to a review by Jaupart et al. (2015).

constrained over nearly 40% of Earth's history. A recent study considered the time-dependence of internal heating but not of CMB temperature (O'Malley et al., 2024). The effect of secular cooling on global heat transfer and mantle dynamics becomes increasingly important in earlier geological times. Extending reconstructions of past plate motions from the past billion years (Merdith et al., 2021) to the past 1.8 Gyr (Cao et al., 2024) enables simulations of mantle convection and the effects of secular cooling over nearly 40% of Earth's history. A coupled core-mantle thermal evolution model modified from Labrosse (2015) suggests that CMB temperature may have decreased by up to 12% from 1.8 Ga (Fig. S1), potentially resulting in a significant effect on models of past mantle convection.

The evolution of CMB heat flow reflects the coupling between Earth's two gigantic heat engines: convection in the mantle and convection in the core, which can generate dynamo action (e.g., Olson, 2016). CMB heat flux influences mantle plume generations, which transport heat from the deep Earth to the surface (e.g., Li et al., 2018; Zhong, 2006). Mantle plumes rising from the CMB are thought to cause Large Igneous Provinces (LIPs) (e.g., Richards et al., 1989; Campbell, 2005), and the LIP record has been used to infer past plume activity (e.g., Ernst, 2014), although how closely CMB heat flux correlates with plume activity is debated (e.g., Labrosse, 2002; Li et al., 2018). LIP activity from 160 Ma appears to be inversely correlated with CMB heat flux inferred from geomagnetic reversal rates (e.g., Olson and Amit, 2015), and 2D geodynamic models (e.g., Li et al., 2018) suggest a first-order correlation between total plume heat flux and total CMB heat flux.

In this study, we carry out thermochemical mantle convection calculations driven by plate motion history models (from Müller et al., 2022 and Cao et al., 2024) to investigate how a decreasing CMB temperature and a decreasing internal heating rate affect the secular variation of CMB heat flux, total plume heat flux, the area of basal mantle structures or Big LOwer-mantle Basal Structures (BLOBS; Cucchiaro et al., 2025), and the number of LIPs through time.

2. Methods and setup

We implemented secular cooling in a version of the mantle convection code CitcomS (Zhong et al., 2008) modified to read in temperature boundary conditions from tectonic reconstruction models (Bower et al., 2015). We used CitcomS to solve the equations of conservation of mass, momentum, and energy under the extended Boussinesq approximation in a 3D spherical model domain. Under this approximation, viscous dissipation, an adiabatic temperature gradient, internal heating and a depth-dependent coefficient of thermal expansion are considered. Details of the governing equations can be found in Zhong (2008).

2.1 Paleogeographically constrained mantle flow models

We considered plate tectonic reconstructions from Müller et al., 2022 (called M22 hereafter), extending back to 1 Ga and from Cao et al., 2024 (called C24 hereafter), extending back to 1.8 Ga. C24 is the first continuous global plate tectonic reconstruction model spanning nearly 40% of Earth's history. It was developed by integrating geological and geophysical data and spans the last three supercontinents, providing a tectonic framework to analyze long-term mantle convection. We modified C24, from its original paleomagnetic reference frame to an optimized reference frame (OPT) that minimise lithospheric net rotation, trench migration rate, and continental speed, which is appropriate to model mantle convection (Müller et al., 2022).

The models were formulated in a full spherical domain divided into 12 equal-volume caps, each consisting of 128 × 128 × 64 elements. The model was computed using $12 \times 4 \times 4 \times 2$ processors. The resolution was ~$50 \times 50 \times 15$ km near the surface and ~$28 \times 28 \times 27$ km near the CMB. The chemically distinctive basal mantle layer was initially laterally uniform and 113 km thick (2% of the volume of the mantle, Hernlund and Houser, 2008). The plate velocity, thermal structure of the lithosphere, and velocity and thermal structure of subducting slabs were assimilated progressively using a half-space cooling model in the convection models (Bower, 2015). A constant temperature $T = 15$ ºC and time-dependent kinematic boundary conditions derived from plate motion history were imposed at the surface. The temperature was either constant or time-dependent at the CMB (see Section 2.2), at which the velocity boundary condition was free-slip.

Convective vigour was controlled by the Rayleigh number $Ra = \frac{\rho_0 g \alpha_0 \Delta T h^3}{\eta_0 \kappa_0}$, where ρ_0, α_0, η_0, κ_0 were dimensional reference values for density, coefficient of thermal expansion, viscosity, and thermal diffusivity (Table 1). h was the thickness of the mantle. g was the gravitational acceleration. ΔT was the dimensional temperature change across the mantle (the initial ΔT for each case is listed in Table S2), which could decrease with time decreasing the effective *Ra*. For the reference case, *Ra* was equal to 1.20×10^8(the initial *Ra* for each case is listed in Table 2).

Viscous dissipation was controlled by the dissipation number $Di = \frac{R_0 g \alpha_0}{C_{P0}}$, where C_{P0} was the reference heat capacity. The density contrast between the basal mantle material and background mantle was determined by the buoyancy number $B = \frac{\Delta\rho}{\rho_b \alpha_b \Delta T}$, where α_b was the average thermal expansivity in the deep mantle and $\frac{\Delta\rho}{\rho_b}$ was the relative intrinsic density contrast between the two materials. A buoyancy number equal to 0.375 represented basal mantle material ~1.6% denser than background mantle.

Viscosity depended on depth, composition, temperature and pressure:

$$\eta = \eta(r)\eta_C exp\left\{\frac{E_\eta + \rho_0 g Z_\eta (R_0 - r)}{R(T + T_{\text{off}})} - \frac{E_\eta + \rho_0 g Z_\eta (R_0 - R_C)}{R(T_{CMB} + T_{\text{off}})}\right\},$$

where *r* was the radius, and the depth-dependent pre-factor was $\eta(r) = 1.4 \times 10^{19}$ Pa s above 160 km (lithosphere) and between 310–660 km depth, $\eta(r) = 4.3 \times 10^{17}$ Pa s between 160–310 km depth (asthenosphere), and $\eta(r) = 4.3 \times 10^{20}$ Pa s below 670 km depth (lower mantle). The compositional pre-factor η_C was equal to 100 for the continental lithosphere and equal to 10 for the basal layer. R_C was the radius of the core, E_η was the activation energy, *R* was the universal gas constant, Z_η was the activation volume, *T* was the dimensional temperature, $T_{\text{off}} = 0.16\,\Delta T_0$ was a temperature offset, and ΔT_0 was the initial temperature difference between the core-mantle boundary and the surface, which varied across models (Table S2).

Table 1. Fixed non-dimensional and dimensional model parameters.

Parameter	Symbol	Value
Reference thermal expansivity	α_0	3.0×10^{-5} K^{-1}
Reference thermal expansivity around the CMB	α_b	1.32×10^{-5} K^{-1}
Reference density	ρ_0	4000 kg m^{-3}
Acceleration of gravity	g	9.81 m s^{-2}
Radius of the Earth	R_0	6371 km
Radius of the Core	R_C	3504 km
Mantle thickness	h	2867 km
Reference heat capacity	C_{P0}	1200 J kg^{-1} J^{-1}
Reference viscosity	η_0	7.16×10^{20} Pa s
Reference thermal diffusivity	κ_0	1×10^{-6} m^2 s^{-1}
Dissipation number	Di	0.71
Buoyancy number	B	0.375
Activation energy	E_η	284 kJ mol^{-1}
Universal gas constant	R	8.31 J mol^{-1}K^{-1}
Activation volume	Z_η	2.1×10^{-6} m^{3}mol^{-1}

Table 2. Parameters varied across model cases.

Model case	***a₀* *(Ga)***	**Plates**	***H* (TW)**	**T_{CMB} (K)**	***Ra***
C-H_c-1	1	M22OPT	13	3391	1.20×10^8
I-H_t-1	1	M22OPT	13(t)	Imposed	1.28×10^8
S_{60}-H_t-1.8-Lo	1.8	C24OPT	13(t)	Self-consistent (60)	1.36×10^8
S_{90}-H_t-1.8	1.8	C24OPT	13(t)	Self-consistent (90)	1.29×10^8
S_{60}-H_t-1.8-Hi	1.8	C24OPT	13(t)	Self-consistent (60)	1.46×10^8

2.2 Secular cooling

2.2.1 Core energy balance framework

To ascertain the effect of secular cooling, we implemented time-dependent CMB temperature (T_{CMB}) and internal heating rate H into the model. Time-dependent T_{CMB} was consistent with the CMB total heat flow according to a simplified core energy balance equation (e.g., Gubbins et al., 2003; Nimmo, 2015):

$$Q_{\mathrm{CMB}} = -C\frac{dT_{\mathrm{CMB}}}{dt}, \quad (1)$$

where C was the effective total heat capacity of the core, t was time, and $T_{CMB} = \Delta T + 288$ K, where ΔT was the temperature difference across the mantle (input parameter into the mantle flow model) and 288 K is the assumed surface temperature.

2.2.2 Implementation of self-consistent T_{CMB}

In a core energy balance equation without radioactive heating the total heat flow across the CMB (Q_{CMB}) is proportional to the core cooling rate (e.g., Gubbins et al., 2003; Nimmo, 2015). We updated T_{CMB} using Eq. 1 with Q_{CMB} computed from the previous model timestep, so that T_{CMB} was self-consistent with Q_{CMB}: $T_{\mathrm{CMB\,(new)}} = T_{\mathrm{CMB\,(old)}} - \frac{Q_{\mathrm{CMB\,(old)}}}{C}$, where 'new' indicated quantities at the current timestep and 'old' indicated quantities at the previous timestep.

The heat capacity of the core (e.g., Butler et al., 2005) increased significantly from the onset of inner core crystallization. The specific heat capacity by unit mass of the core is usually assumed to have been constant before inner core crystallization, ranging from 715 J kg^{-1} K^{-1} to 930 J kg^{-1} K^{-1} (see Nimmo, 2015, for a review). Multiplying the specific heat capacity by unit mass by the mass of the core (1.93×10^{24} kg), and converting seconds to million years, we obtained C ≃ 60 TW Myr^{-1} K^{-1} for the maximum effective total heat capacity of the core before inner core crystallization. Thermal evolution calculations for the core (Fig. S1) suggest that C could be as large as 90 TW Myr^{-1} K^{-1} after inner core crystallization. We used C = 60 TW Myr^{-1} K^{-1} for most cases and considered a case (S_{90}-H_t-1.8) with C = 90 TW Myr^{-1} K^{-1}.

2.2.3 Implementation of decreasing internal heating rate based on radiogenic decay

To examine the effect of secular cooling, we implemented a decreasing internal heating rate in the model (Fig. 2b) following the evolution of radiogenic heat production, defined as:

$$H(t) = H(0)\sum_{n=1}^{4} h_n exp(\lambda_n t),$$

where $H(0)$ was the radiogenic heat production at present (Table 2), t was the time before present, h_n was the weighted heat generation rates of radiogenic isotopes according to their relative natural concentrations, and λ_n was the radioactive decay constant which described isotope decay rates (Table S1; Korenaga, 2006).

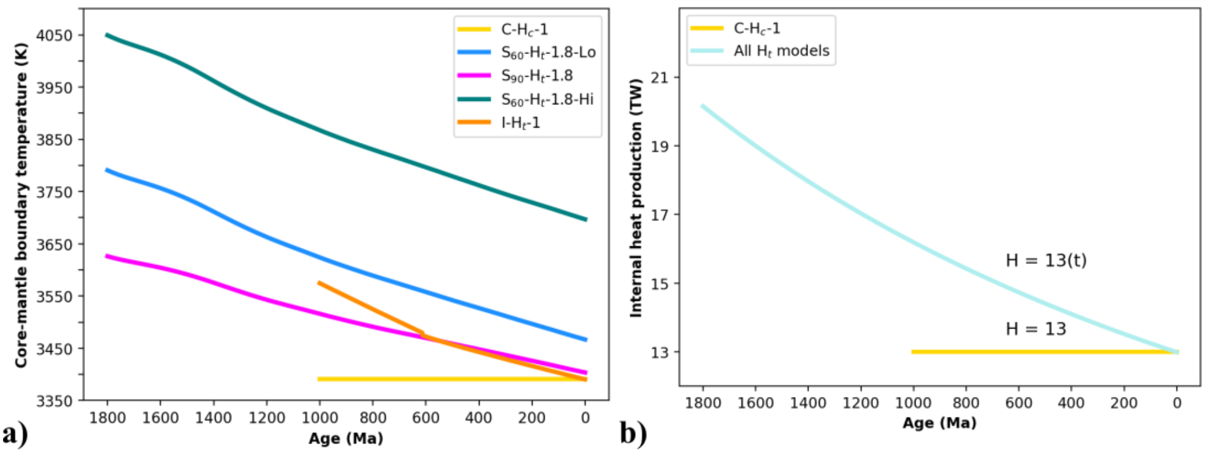

Figure 2. a) Evolution of CMB temperature. **b**) Evolution of internal heating across the considered model cases.

2.3 Considered model cases

Model case names generally consist of three parts separated by hyphens: the first part indicates T_{CMB} to be either constant ('C'), imposed ('I') or self-consistent ('S_{60}' for $C = 60$ TW Myr^{-1} K^{-1} or 'S_{90}' for $C = 90$ TW Myr^{-1} K^{-1}); the second part indicates H to be either constant (H_c) or time-dependent (H_t); the third part indicates the start age a_0 to be either 1 Ga ('1') or 1.8 Ga ('1.8'). One model contains a fourth part ('Hi') to indicate a larger Ra (Table 2). In the reference case (C-H_c-1) T_{CMB} and the internal heating rate H were constant. We considered a model case (I-H_t-1) in which T_{CMB} was imposed (Fig. 2a) and H decreased over time to assess the contribution of secular cooling to the surface and CMB heat flow. The effect of the effective heat capacity of the core on the cooling rate can be inferred from cases

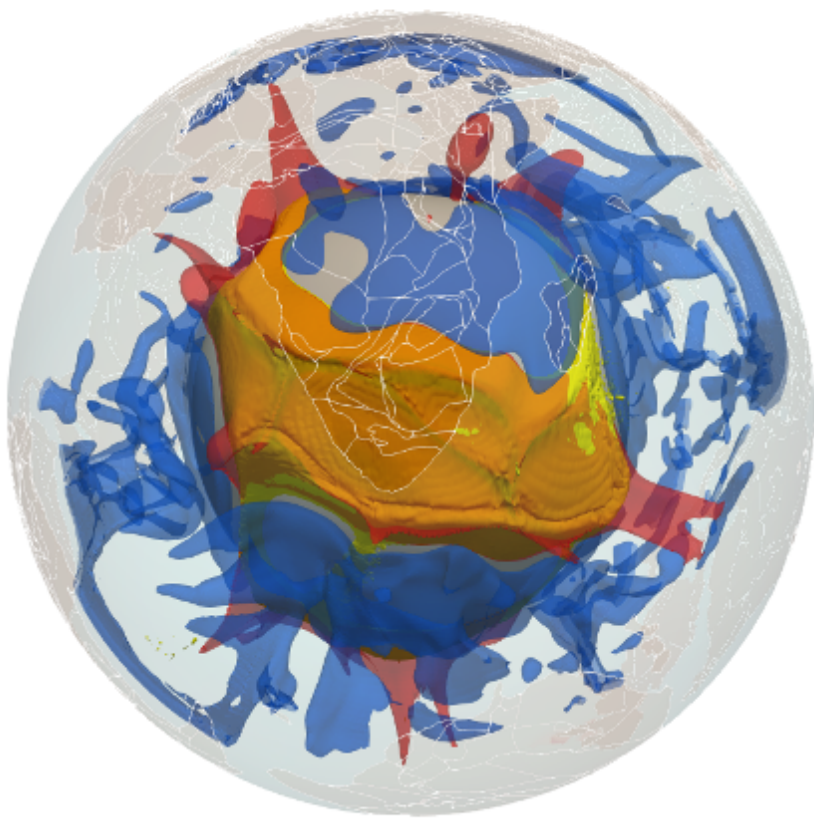

Figure 3. 3D snapshot of reference model case C-H_c-1 at present-day. At the surface, the transparent brown polygons with white outlines show continents. Blue and red surfaces are 217 K colder-than-average and 372 K warmer-than-average, respectively. Golden regions are BLOBS, with orange showing the overlap of BLOBS and hotter-than-average areas.

S_{60}-H_t-1.8-Lo and S_{90}-H_t-1.8. *Ra* was adjusted (for example between S_{60}-H_t-1.8-Hi and S_{60}-H_t-1.8) so that models reached similar present-day CMB temperature (Fig. 2a).

2.4 Quantifying model success

Match to tomography and volcanic eruptions. We computed the fractional area f_a of Earth's surface covered by BLOBS (or LLSVPs) identified from two-means clustering (e.g., MacQueen, 1967) of temperature (or seismic velocity anomalies) between 1,000–2,800 km depth (e.g., Flament et al., 2022) in mantle flow models. We analysed four quantities to evaluate the fit of basal mantle structures to seismic tomographic models and volcanic eruption locations

(Flament et al., 2022): (i) f_a; (ii) $\overline{Acc}$, the average spatial match between cluster maps of present-day BLOBS and LLSVPs imaged by seven global S-wave tomographic models: SEMUCB-WM1 (French and Romanowicz, 2014), Savani (Auer et al., 2014), S40RTS (Ritsema et al., 2011), GyPSuM-S (Simmons et al., 2010), S362ANI (Kustowski et al., 2008), SAW24B16 (Mégnin and Romanowicz, 2000), and HMSL-S (Houser et al., 2008).; (iii) S, the average sensitivity between cluster maps of present-day BLOBS and LLSVPs imaged by seismic tomographic models, defined as $S = TP/(TP + FN)$, where *TP* was the area of true positives and *FN* is the area of false negatives; (iv) $\tilde{\theta}$, the time averaged mean of minimum angular distance between reconstructed volcanic eruption locations and BLOBS, with the distance considered equal to zero for eruption locations above BLOBS and positive for eruption locations outside BLOBS.

Match between plume flux and number of LIPs. Following Labrosse (2002), Zhong et al. (2006) and Li et al. (2023), plumes were defined at each depth and time as regions with upward radial velocity where the temperature satisfied: $T \geq T_{bg} + f(T_{max} - T_{bg})$, where T_{bg} was the average temperature of hotter-than-average areas, T_{max} was the maximum temperature, f = 0.2 was a pre-factor. The total heat flux carried by plumes at a given depth and time was defined as: $Q_p = \int_S q_{\mathrm{adv}} dS$, where S was the area of plumes that satisfied $T - T_{bg} \geq f(T_{max} - T_{bg})$, and q_{adv} was the convective heat flux, defined as: $q_{\mathrm{adv}} = \rho C_p (T - T_{bg}) v_r$, where ρ and C_p were density and heat capacity at the depth, respectively, and v_r was the plume velocity in the radial direction. We normalized the total plume heat flow by the total CMB heat flow at each time and compared it to the number of LIPs through time from three LIP databases (‘D20’, Doucet et al., 2020; ‘EY17’, Ernst and Youbi, 2017; ‘J18’, Johansson et al., 2018).

Urey ratio. The Urey ratio indicated the contribution of radiogenic heat production within the convecting mantle to the convective heat loss at the surface (Christensen, 1985):

$$Ur = \frac{H(t)}{Q(t)},$$

where *Ur* was the Urey ratio, $H(t)$ was the temporal mantle internal heating, and $Q(t)$ was the temporal convective surface heat loss. The Urey ratio provided insight into how Earth's interior cools over time. The Urey ratio should be between 0.2 and 0.4 to be consistent with estimates of Earth's mantle radiogenic production (8–13 TW) and estimated cooling rate (Korenaga, 2008).

2.5 Periodicity detection

We produced Lomb–Scargle (e.g., Lomb, 1976; Scargle, 1982) periodograms, which detects periodic signals by fitting sinusoidal models to unevenly sampled time series through least-squares optimization, from detrended and normalised LIP and plume heat flux time series from 360 Ma. We high-passed filtered the signal to retain periods greater than 30 Myr, and smoothed them using a Savitzky–Golay filter (Savitzky and Golay, 1964) for third-order polynomials.

3. Results

For the reference case, the present-day surface heat flow was equal to 37.9 TW (Fig. 4a), which was consistent with the estimated heat flow from the convecting mantle (36–42 TW, Jaupart et al., 2007). The horizontally averaged mantle temperature at different depths varied by less than 4% over time (Fig. 5a), reflecting that the model evolved smoothly. The calculated present-day total heat flow across the CMB was equal to 12.97 TW (Fig. 4a), which was within the range of 5–15 TW estimated from core thermodynamics (Jaupart et al., 2007). The CMB heat flow increased from 8.3 TW to 15 TW between 1 Ga and 500 Ma, then gradually decreased to 13 TW and varied within 10% of 13 TW from 250 Ma, suggesting an approximate balance ('dynamic equilibrium') between internal heat production, surface heat loss, and basal heat flux.

The computed present-day fractional area of BLOBS was 37.4% (Fig. 4b), which was consistent with tomographic models (between 31.5% and 51.6%). The time evolution of BLOBS area was anti-correlated with the time evolution of the CMB heat flow: f_a decreased from 1 Ga to 500 Ma and then increased until it reached quasi-equilibrium at around 250 Ma. This anti-correlation was expected as CMB heat flow is low through BLOBS, across which temperature gradients are relatively small. The anti-correlation between BLOBS area and CMB heat flow reflected the imposed tectonic history and model parameters including convective vigour and viscosity. The Urey ratio averaged over time for model C-H_c-1 was equal to 0.31, reaching 0.33 at present day, which was close to the value range of 0.2-0.3 suggested by geochemistry (e.g., Korenaga, 2008). The Urey ratio was generally larger in the past (with a maximum of 0.39 at 0.7 Ga; Fig. 4c) and decreased over time, consistent with secular cooling (e.g., Korenaga, 2017).

The present-day CMB heat flow in model I-H_t-1 (in which secular cooling was considered) was 30% lower than that in the reference case (Fig. 4a). This emphasized the effect of secular cooling on CMB heat flow. We therefore focused on model cases with secular cooling.

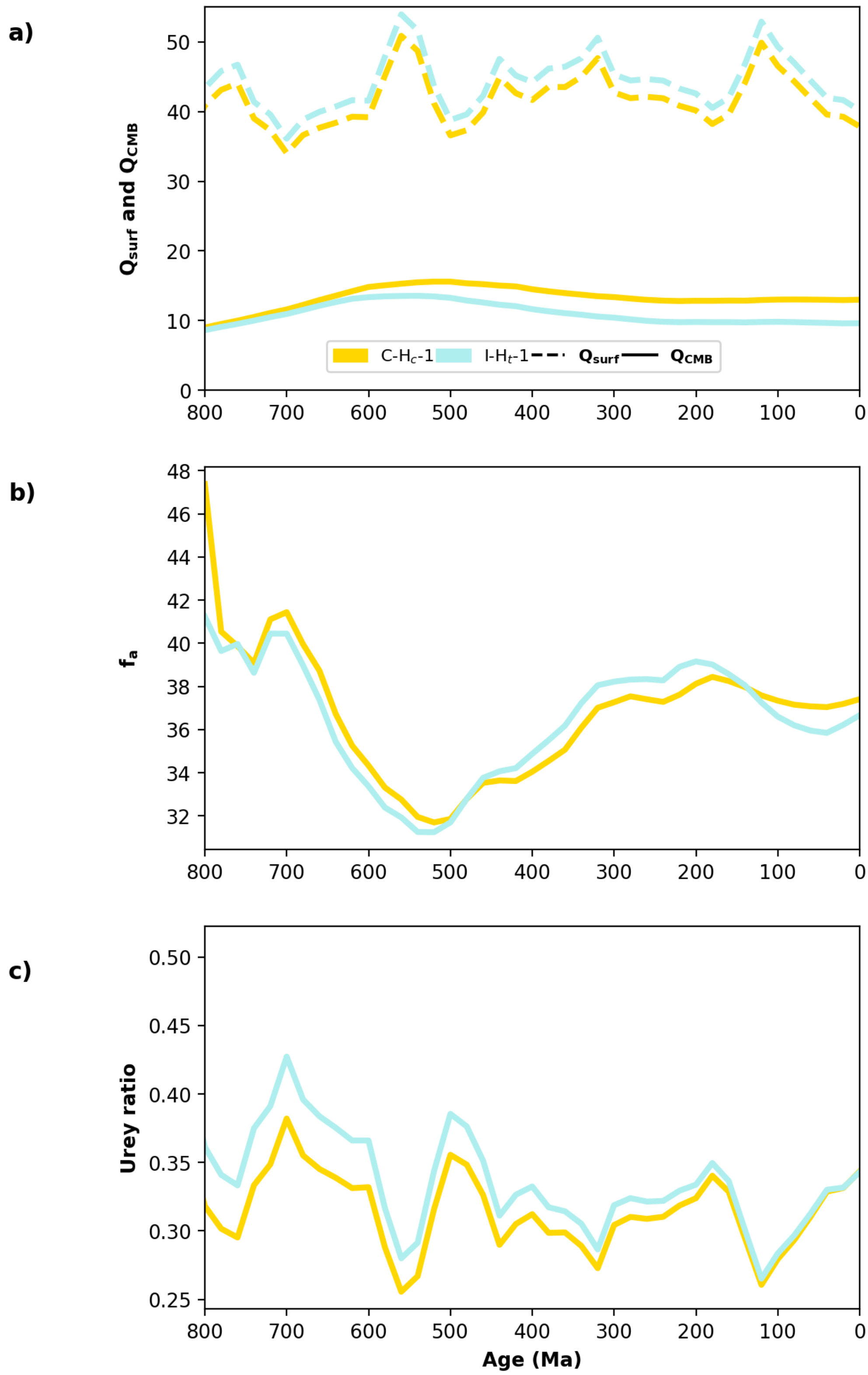

Figure 4. Results for reference case C-H$_c$-1 (gold lines) and I-H$_t$-1 (cyan lines). **a)** Total heat flow across the surface (dashed line, imposed) and CMB (solid line) over time. **b)** Fractional area of BLOBS f_a as a function of time. **c)** Urey ratio over time.

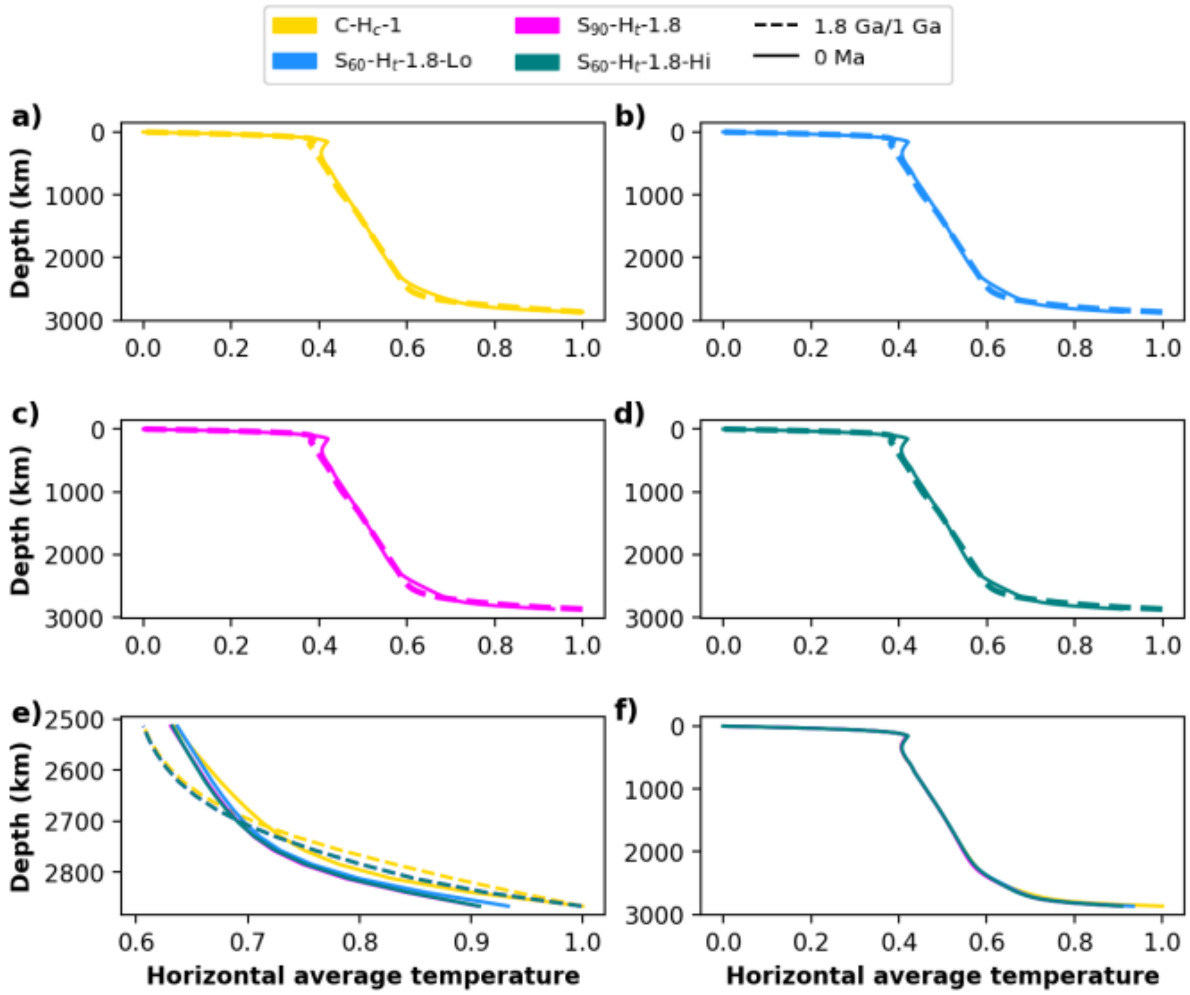

Figure 5. Evolution of non-dimensional horizontal average temperature (in the initial condition and at the present-day) for models C-H$_c$-1 (**a**), S$_{60}$-H$_t$-1.8-Lo (**b**), S$_{90}$-H$_t$-1.8 (**c**), and S$_{60}$-H$_t$-1.8-Hi (**d**), respectively. The initial temperature profiles are very similar across all models. **e)** Lowermost mantle initial and present-day horizontal average temperature. **f)** Present-day horizontal average temperature for the four considered models.

3.1 Effects of secular cooling on CMB heat flow and BLOBS area

We considered model cases extending back to 1.8 Ga, which were driven by reconstruction C24. The horizontally-averaged temperature at different depths were the same at initial time but the lowermost mantle was cooler at present-day in models with secular cooling (Fig. 5). As with the reference model C-H_c-1 (Figs. 4b and 4c), Q_{CMB} increased when f_a decreased in models S_{60}-H_t-1.8-Lo, S_{90}-H_t-1.8, S_{60}-H_t-1.8-Lo, and S_{60}-H_t-1.8-Hi. Our results suggested that it took about 800 Myr for Q_{CMB} to reach dynamic equilibrium, following a phase of large, opposite changes between Q_{CMB} and f_a (Figs. 6a and 6b). From 1.8 Ga to 1.4 Ga, Q_{CMB} more than doubled, reaching a maximum around 1.4 Ga, while f_a decreased sharply by 30%. From around 1,000 Ma, as Q_{CMB} reached quasi-equilibrium, f_a oscillated by ±7.5% around 35%, varying inversely with Q_{CMB}.

Increasing C from C $\simeq$ 60 TW Myr^{-1} K^{-1} (S_{60}-H_t-1.8-Lo) to C $\simeq$ 90 TW Myr^{-1} K^{-1} (S_{90}-H_t-1.8) decreased the CMB cooling rate from 180 K Gyr^{-1} to 123 K Gyr^{-1} (Fig. 2a). Increasing convective vigour modified the cooling rate, as expected. The cooling rate was 180 K Gyr^{-1} for case S_{60}-H_t-1.8-Lo and 196 K Gyr^{-1} for case S_{60}-H_t-1.8-Hi (Fig. 2a). For these two cases, the present-day T_{CMB} was equal to 3,467 K (Case S_{60}-H_t-1.8-Lo) and to 3,697 K (Case S_{60}-H_t-1.8-Hi), respectively. T_{CMB} and Q_{CMB} were ~9.5% greater in model S_{60}-H_t-1.8-Hi than in model S_{60}-H_t-1.8-Lo for all times (Fig. 2a and Fig. 6b).

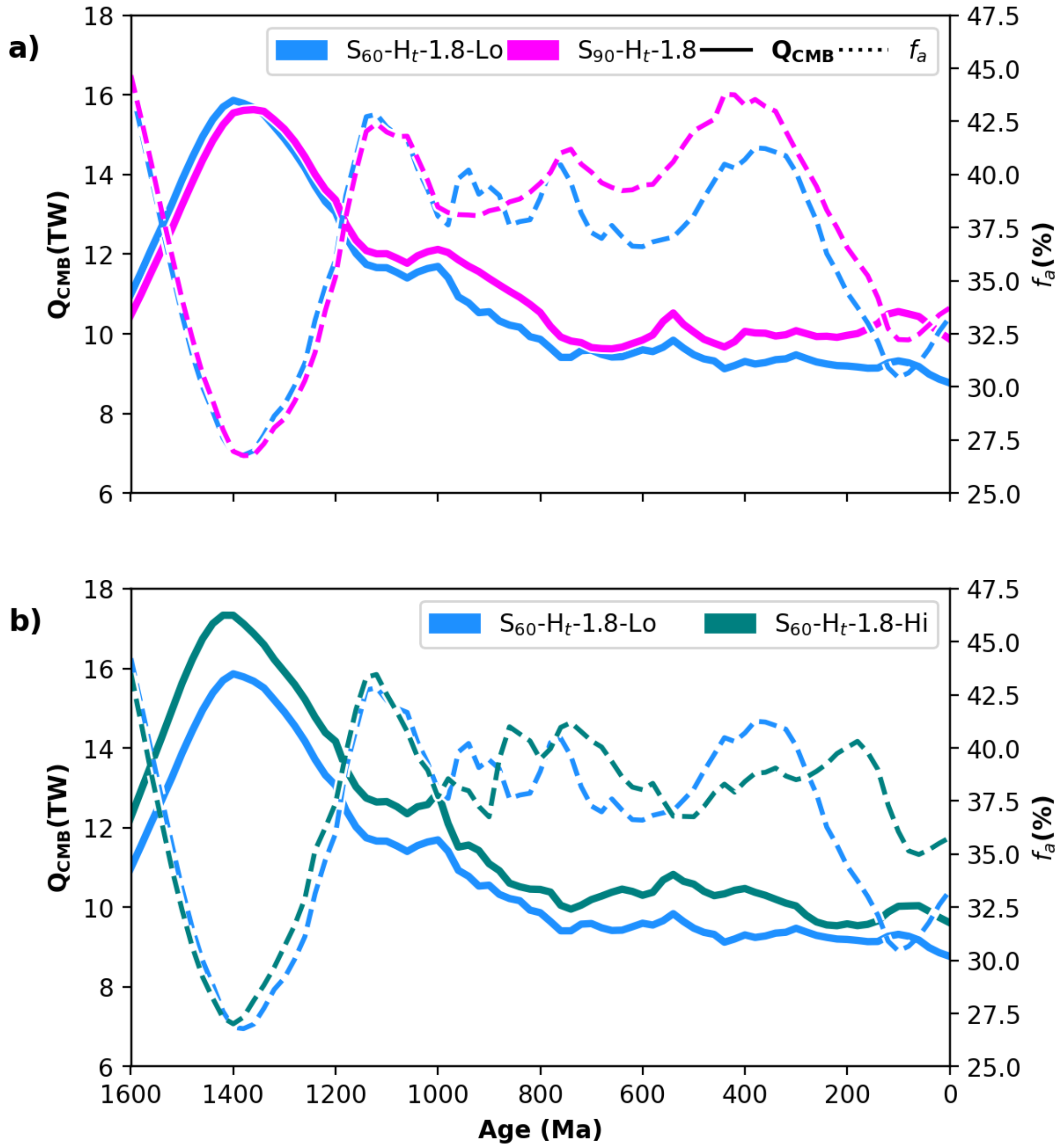

Figure 6. CMB heat flow Q_{CMB} and BLOBS fractional area f_a as a function of time. **a)** Results for cases S_{60}-H_t-1.8-Lo, and S_{90}-H_t-1.8, illustrating the effects of self-consistent T_{CMB}, with different core thermal conductivity. **b)** Results for cases S_{60}-H_t-1.8-Lo, and S_{60}-H_t-1.8-Hi, illustrating the effects of greater convective vigour. Solid lines show Q_{CMB} and dashed lines represent f_a. Model cases are color-coded.

3.2 Effects of secular cooling on model success

We evaluated model success and parameter trade-offs from f_a, ($\overline{Acc}$), (S), and ($\tilde{\theta}$) (see Section 2.7). For tomographic models, the fractional area was $0.315 < f_a < 0.52$, with median f_a equal to 0.34 (Fig. 7a). For mantle flow models, it was $0.3 < f_a < 0.4$ for all cases and f_a fell outside the tomographic range only for the reference case C-H_c-1 ($f_a = 0.311$) (Fig. 7a). f_a was closer to the median of tomographic models for models using reconstructed plate history extending back to 1.8 Ga.

The accuracy was $0.73 < \overline{Acc} < 0.88$ across tomographic models, with median $\overline{Acc}$ = 0.828 (Fig. 7b). A large accuracy indicates a good match between a given model and all considered tomographic models. The reference model case C-H_c-1 yielded $\overline{Acc}$ within the range of tomographic models ($\overline{Acc} = 0.80$, Fig. 7b). However, in the 1.8 Ga models, the accuracy was lower than 0.73 except for model S_{60}-H_t-1.8-Hi, for which it was equal to 0.75, within the range of tomographic models (Fig. 7b).

The sensitivity was $0.62 < S < 0.82$ for tomographic models, with the median $\overline{S}$ = 0.77 (Fig. 7c). Larger sensitivities indicated a better the spatial match between BLOBS and LLSVPs for a given model and tomographic models. For the reference case C-H_c-1 the sensitivity was equal to 0.70, which was within the range of results for tomographic models (Fig. 7c). In the 1.8 Ga models, sensitivity was the largest for case S_{60}-H_t-1.8-Hi.

The time-averaged mean distance from volcanic eruptions to BLOBS was $2.79° < \tilde{\theta} < 9.33°$ across tomographic models, with the median equal to 6.73° (Fig. 7d). Smaller time-averaged mean distance from volcanic eruptions indicated models that were most consistent with volcanic eruptions, assuming a link between BLOBS or LLSVPs and surface volcanic eruptions (Torsvik et al., 2010; Flament et al., 2022; Müller et al., 2022; Cucchiaro et al., 2025). This range was larger for the 1.8 Ga models ($5.91° < \tilde{\theta} < 9.19°$, Fig. 7d). The angular distance most comparable to tomographic models was obtained for cases S_{60}-H_t-1.8-Lo and S_{60}-H_t-1.8-

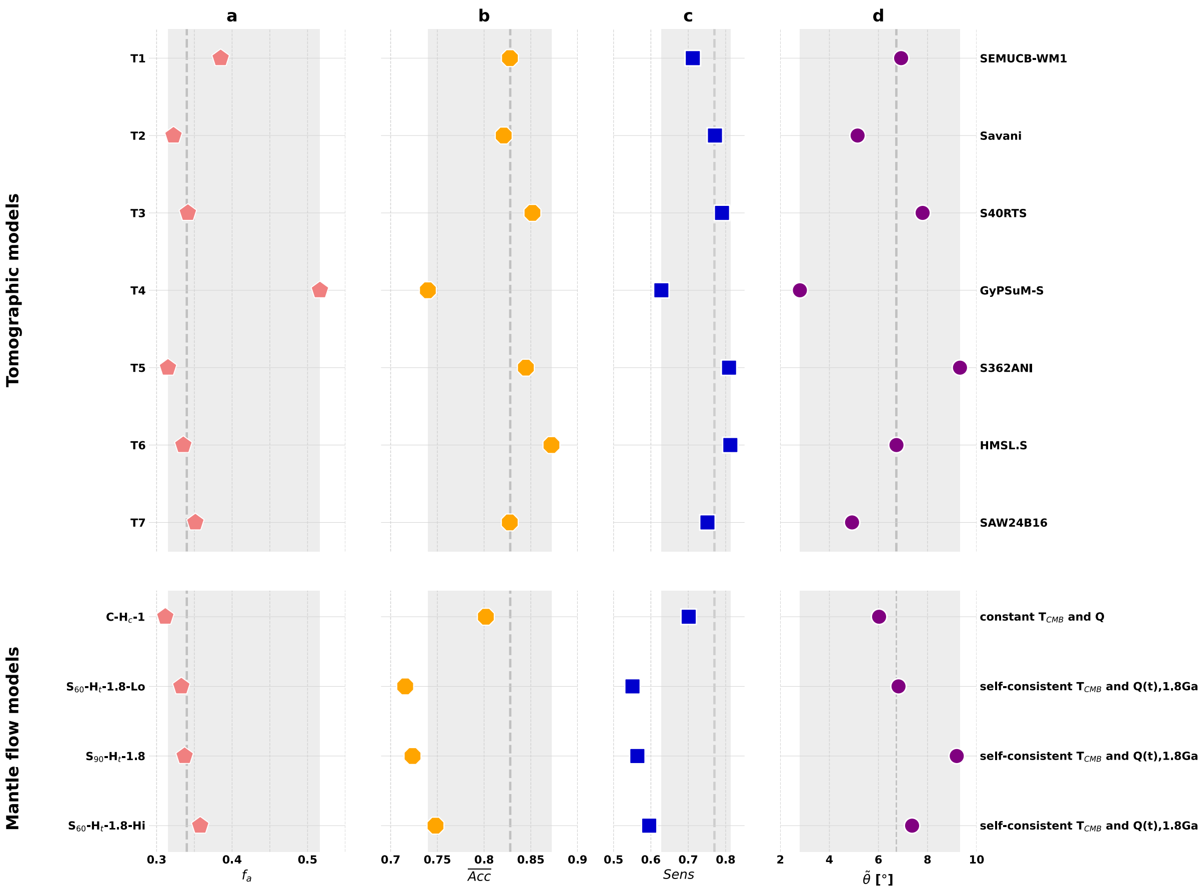

Figure 7. Fit of basal mantle structures from global mantle flow models to seismic tomography models and volcanic eruption locations. **a)** f_a, fractional area of deep mantle cluster maps between 1000 km and 2800 km depths covered by slow (in tomography) or hot (at present-day in mantle flow models) BLOBS. **b)** $\overline{Acc}$**,** averaged spatial match between present-day BLOBS for a given model and tomographic models T1-T7. **c)** *S*, averaged sensitivity of present-day BLOBS for a given model to tomographic models T1-T7. **d)** $\tilde{\theta}$, mean of minimum angular distance averaged from 320 Ma between volcanic eruption locations and BLOBS edges. The top panel presents results for a wide range of tomographic models T1-T7. The bottom panel exhibits results for global mantle flow models investigated in this study. Grey shaded areas marked the range of metrics for tomographic models T1-T7 (for $\overline{Acc}$ and *S,* independent tomographic models are considered). Grey dashed lines indicated the median of metrics for tomographic models T1-T7.

Hi.

Case S_{60}-H_t-1.8-Hi was the 1.8 Ga model that provided the best joint fit to tomography and surface volcanism. This could be verified by the similarity between the cluster maps (1,000-2,800 km depths) of case S_{60}-H_t-1.8-Hi and tomographic models at 320 million years ago and at present-day (Fig. S3).

3.3 Temporal evolution and periodicity of plume heat flow

We analysed the temporal variation of the total heat flux carried by plumes (defined in Section 2.5) at 1,040 km depth normalized by Q_{CMB} (dashed lines in Fig. 8a). We compared the predictions for cases C-H_c-1, S_{90}-H_t-1.8, and S_{60}-H_t-1.8-Hi, to the number of LIP occurrences in the geologic record. Results for the other case were generally similar to these three models, with some second-order differences (Fig. S2). There were two peaks in the two 1.8 Ga models around 1400 Ma and one around 150 Ma, and two peaks around 600 Ma and 150 Ma in case C-H_c-1 (Fig. 8a). The first peak occurred 400 million years after the start of the main calculation. We compared the secular variation of total plume flux with three LIP databases (Doucet et al., 2020; Ernst and Youbi, 2017; Johansson et al., 2018) resampled in 20-million-year intervals and plotted at the younger age boundary of each bin (coloured shaded areas in Fig. 8a). This revealed a peak in LIP occurrence between 140 and 120 Ma that was predicted by the deep mantle heat flux in all three mantle flow models, as agreed by all three sets of LIP records. LIP records essentially showed a bilateral peak feature to the first order, which was similar to the predicted plume flux variation.

We analysed the periodicity of plume heat flux for LIP databases EY17, J18 and D20 and for model cases C-H_c-1, S_{90}-H_t-1.8, and S_{60}-H_t-1.8-Hi between 360 Ma and the present day. We focused on periods longer than 60 Myr because data were generally sparse, and mantle flow models were analysed in 20 Myr increments. The comparison was most favourable between

D20 LIPs with significant power at periods ~71 Myr, ~97 Myr and ~156 Myr, and C-H_c-1 with significant power at periods ~73 Myr, ~103 Myr, and ~144 Myr (Fig. 8b). LIP databases differed by the presence of eruptions associated with mantle plume conduits (in J18) and the addition of oceanic LIPs in deep time (in D20), or with silicic LIPs (in EY17). Such differences may explain the differences in dominant period in EY17 (~65 Myr, which is consistent with the analysis by Prokoph et al., 2013), J18 (~88 Myr) and D20, (~97 Myr). The parameters of mantle flow models, including the presence or absence of secular cooling, affect total plume heat flux, reflecting the differences in dominant period in model cases C-H_c-1 (~103 Myr), S_{90}-H_t-1.8 (~116 Myr), and S_{60}-H_t-1.8-Hi (~124 Myr).

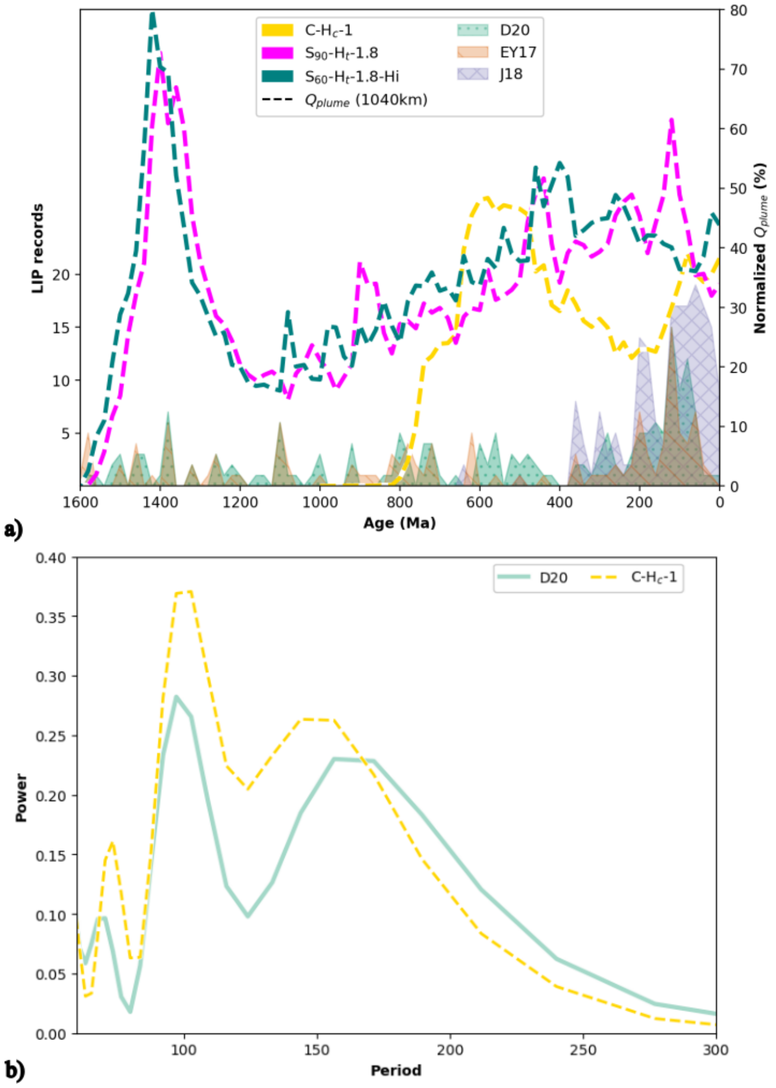

Figure 8. Heat flux carried by lower mantle plumes at 1,040 km depth normalized by Q_{CMB}, compared with LIP records (from 'D20': Doucet et al., 2020; 'EY17': Ernst and Youbi, 2017; and 'J18': Johansson et al., 2018). **a)** Plume flux predicted by mantle flow models and LIP records. Plume flux is represented by dashed lines, with colours indicating model cases. The green dotted area represents LIPs from Doucet et al. (2020). The orange hatched area represents LIP records from Ernst and Youbi (2017). The purple cross-hatched area indicates LIP records from Johansson et al. (2018). **b)** Processed periodogram for plume flux from 0–360 Ma for case C-H_c-1 and LIP record from Doucet et al. (2020) (only periods ≥ 60 Myr are shown). Dashed lines represent periodicity for plume flux, with colour meanings consistent with that in **a**). The solid line represents the periodicity for the LIP record.

4. Discussion

Our global thermochemical convection models demonstrate that incorporating secular cooling fundamentally alters the long-term evolution of deep mantle structure and heat transfer. By imposing or self-consistently calculating a decreasing CMB temperature and declining internal heating, we show that the balance among basal heating, internal heat production, and surface heat loss evolves in ways not captured by models that assume constant boundary conditions.

Our models consistently showed a ∼800 Myr transient phase in models extending back to 1.8 Ga. During this period, the CMB heat flux increases sharply as slabs reorganize and deform the basal thermochemical layer, after which the system relaxes toward a quasi-steady thermal regime. The transient phase was ~50 Myr long for one model case with a dense basal layer and > 200 Myr long for a model case without dense basal layer in models by Flament et al. (2014) that did not account for secular cooling, dissipation, or an adiabatic gradient. In our models, the duration of the initial transient phase is expected to depend on convective vigour (Rayleigh number), viscosity, initial condition (initial slab depth, presence of a dense basal layer) and the tectonic reconstruction. The duration of this transient phase should be characterised and taken into account when interpreting the results of forward global mantle flow models. A strategy to reduce the duration of the initial transient phase it to use a warm-up phase (e.g., Frasson et al., 2024).

The anti-correlation between CMB heat flux and the fractional area of BLOBS is a robust and persistent feature across all models. As slabs impinge on the basal thermochemical layer, BLOBS are compressed and displaced, reducing their area and increasing CMB heat flow. This behaviour is consistent with earlier 2D and 3D thermochemical models showing that the geometry of dense basal structures strongly modulates deep-mantle heat transfer (e.g., Nakagawa and Tackley, 2004; Li et al., 2018; Nakagawa and Tackley, 2008). In 3D spherical geometry, these interactions are inherently more complex than in reduced-dimensional models, producing a dynamic interplay among slabs, BLOBS margins, and plume initiation zones.

The relationship between predicted plume heat flux from models and LIP emplacement is broadly consistent but not strictly synchronous. This outcome reflects several factors. First, LIPs are unevenly preserved in the geological record due to subduction, erosion, and tectonic reworking, and published radiometric ages carry uncertainties ranging from several million years to tens of millions of years, particularly for Proterozoic events (e.g., Johansson et al., 2018; Ernst and Youbi, 2017). These uncertainties limit the temporal resolution with which plume-LIP linkages can be assessed. Second, not all plumes produce LIPs – successful LIP generation requires sufficiently high potential temperatures, large buoyancy fluxes, or favourable lithospheric conditions (e.g., Tappe et al., 2018; Doucet et al., 2020). To further assess this broad plume-LIP linkage, we analysed the periodicity of both LIP records and model-predicted plume heat flux. Overall, the periods varied between LIP databases (Fig. S4), which highlighted the relatively short time series, sparse data, and differences between the databases (with or without oceanic plumes in deep time, with or without eruptions associated with plume tails). The dominant period in LIP records J18 and D20 (between ~88–97 Myr) were shorter than in model cases C-H_c-1, S_{90}-H_t-1.8, and S_{60}-H_t-1.8-Hi (between ~103–124 Myr). This could reflect that the model plume heat flux was characterised globally from mantle plume conduits, whereas the LIP record is increasingly biased towards continental eruptions associated with plume heads back in time. We note that the dominant periods predicted by models would change with model parameters. Future work could focus on mantle plume heads predicted by models, although these would be sparse through time.

Our models do not exhibit the quasi-periodic plume pulses observed in many 2D models (e.g., Lin and van Keken, 2005; Olson and Amit, 2015; Li et al., 2018; Heyn et al., 2020). In simplified 2D geometries with free-slip vertical boundaries, slabs descend along the sides of the model domain, forcing plume formation directly above the crest of BLOBS and producing regular oscillatory patterns. In contrast, in 3D spherical models – whether ours or previous studies (Li et al., 2014; McNamara and Zhong, 2004; Hassan et al., 2015; Tan et al., 2011; Cao et al., 2021; Cucchiaro et al., 2025) – plumes can originate above, along, or near BLOBS margins. This geometric freedom suppresses simple thermal resonance behaviour and yields spatially and temporally heterogeneous plume production. Li et al. (2023) further showed that plume periodicities decrease with increasing convective vigour in 3D global convection models, consistent with our finding that decreasing CMB temperature influences the variance of plume activity by reducing convective vigour.

Our modelling framework incorporates a simplified coupling between mantle convection and core energy balance. Unlike more complex formulations (e.g., Nakagawa and Tackley, 2004; Nakagawa and Tackley, 2012), we do not include the onset of inner-core growth or latent heat and gravitational energy release associated with solidification. These additions influence effective core heat capacity but also introduce significant uncertainties in material properties of the deep core. Besides, when assimilating slabs following Bower et al. (2015), the CMB temperature was constant (mean of the present-day and 1.8 Ga) and not updated over time. This may have modestly enhanced mantle circulation and plume flux initially and slightly reduced them later. However, because CMB temperature varied by only ~5% around the applied mean (Fig. 2a), the effect on slab temperature and first-order results is negligible. Despite these simplifications, the cooling rates produced by our models (~123–198 K Gyr^{-1}) fell within the range estimated from Earth's Urey ratio and convective heat flux (Korenaga, 2008) and overlapped the broader range inferred for secular cooling (60–210 K Gyr^{-1}). Although our rates were slightly higher than some geodynamic estimates (e.g., Zhong, 2006; Nakagawa and Tackley, 2004; Nakagawa and Tackley, 2012) and exceeded values inferred from geological proxies (e.g., Abbott et al., 1994; Grove and Parman, 2004; Nisbet and Fowler, 1983), they were consistent with first-order constraints.

Overall, our results demonstrate that self-consistent secular cooling is an essential boundary condition for reconstructing deep mantle evolution, interpreting plume-LIP relationships, and understanding long-term coupling between Earth's core and mantle. Future studies can expand on this framework by incorporating slab-consistent thermal assimilation (Bower et al., 2015), ridge melting and dehydration effects (Korenaga, 2003, 2017), and inner-core growth to further refine Earth's thermochemical history.

5. Conclusions

1. Secular cooling should be included in long-term global mantle flow models. Our 3D global thermochemical convection models incorporating 1.8 billion years of plate motion history demonstrate that secular cooling exerts a first-order influence on deep mantle dynamics and the long-term evolution of the core-mantle system. By explicitly coupling mantle convection with a time-dependent CMB temperature and declining internal heating, we show that the structure and vigour of mantle convection evolve differently from models assuming constant thermal boundary conditions. A consistent feature of all simulations was an extended transient phase during which sinking slabs and the deformation of basal thermochemical structures act to reorganize deep mantle flow before a long-term dynamic equilibrium is established. This behaviour emphasizes the necessity to characterize and use a warm-up phase to fully capture the inherited thermochemical context of the present-day mantle.

2. Slabs–BLOBS interactions control CMB heat flux in a predictable anti-correlation. Secular cooling significantly influences CMB heat flux and the evolution of basal thermochemical structures, producing a persistent anti-correlation between BLOBS area and CMB heat flow. This interaction governs how deep-mantle heterogeneity controls heat transfer

from the core. Our models also show that plume heat flux varies independently of CMB heat flow, reflecting the complex geometry of plume initiation in 3D spherical convection and the non-periodic nature of plume generation under realistic boundary conditions.

3. Broad agreement between predicted plume flux and LIP events. Predicted plume heat fluxes broadly reproduced the long-term distribution of LIP events, though not in a one-to-one fashion, consistent with geological uncertainties, preservation biases, and the selective nature of LIP formation. The resulting cooling rates between ~123–198 K Gyr^{-1} were compatible with geophysical and geochemical estimates, supporting the viability of our simplified coupling approach.

4. Perspectives. Overall, our results emphasize that incorporating self-consistent secular cooling is essential to reconstruct Earth's thermochemical evolution, for interpreting long-term plume and LIP activity, and to understand the interplay between mantle convection and core energetics. The characterisation of periodicities in the volcanic record and in mantle flow models could be refined in future studies. Future work incorporating inner-core growth and upper-mantle dehydration effects could further refine models of Earth's thermal history.

Acknowledgments

Jiaxin Zhang and Nicolas Flament were supported by Australian Research Council (ARC) grant LP220100056 (industry partners: Anglo American and De Beers). Nicolas Flament was supported by ARC FT230100001. The models were performed using computational resources on the National Computational Infrastructure (NCI), which is supported by the Australian Government. Access to NCI was partly supported by resources and services from the University of Wollongong (UOW).

CRediT authorship contribution statement

Jiaxin Zhang: Conceptualization, Investigation, Methodology, Software, Visualization, Analysis, Writing – original draft, Writing – review and editing. **Nicolas Flament:** Conceptualization, Methodology, Analysis, Writing – review and editing, Supervision, Project administration, Funding acquisition. **Stéphane Labrosse:** Methodology, Writing – review and editing, **Xianzhi Cao:** Methodology, Writing – review and editing. **Dietmar Müller:** Methodology, Writing – review and editing. **Annalise Cucchiaro:** Visualization, Writing – review and editing.

References

1. Abbott, D., Burgess, L., Longhi, J., & Smith, W. H. F. (1994). An empirical thermal history of the Earth's upper mantle. *Journal of Geophysical Research: Solid Earth*, *99*(B7), 13835-13850. https://doi.org/10.1029/94jb00112
2. Auer, L., Boschi, L., Becker, T., Nissen-Meyer, T., & Giardini, D. (2014). Savani: A variable resolution whole-mantle model of anisotropic shear velocity variations based on multiple data sets. *Journal of Geophysical Research: Solid Earth*, *119*(4), 3006-3034. https://doi.org/10.1002/2013JB010773
3. Bower, D. J., Gurnis, M., & Flament, N. (2015). Assimilating lithosphere and slab history in 4-D Earth models. *Physics of the Earth and Planetary Interiors*, *238*, 8-22. https://doi.org/10.1016/j.pepi.2014.10.013
4. Butler, S., Peltier, W., & Costin, S. (2005). Numerical models of the Earth's thermal history: Effects of inner-core solidification and core potassium. *Physics of the Earth and Planetary Interiors*, *152*(1-2), 22-42. https://doi.org/10.1016/j.pepi.2005.05.005
5. Campbell, I. H. (2005). Large igneous provinces and the mantle plume hypothesis. *Elements*, *1*(5), 265-269. https://doi.org/10.2113/gselements.1.5.265

6. Cao, X., Flament, N., Bodur, O. F., & Muller, R. D. (2021). The evolution of basal mantle structure in response to supercontinent aggregation and dispersal. *Sci Rep*, *11*(1), 22967. https://doi.org/10.1038/s41598-021-02359-z
7. Cao, X. Z., Collins, A. S., Pisarevsky, S., Flament, N., Li, S. Z., Hasterok, D., & Müller, R. D. (2024). Earth's tectonic and plate boundary evolution over 1.8 billion years. *Geoscience Frontiers*, *15*(6). https://doi.org/10.1016/j.gsf.2024.101922
8. Christensen, U. R. (1985). Thermal evolution models for the Earth. *Journal of Geophysical Research: Solid Earth*, *90*(B4), 2995-3007. https://doi.org/10.1029/JB090iB04p02995
9. Cucchiaro, A., Flament, N., Arnould, M., & Cressie, N. (2025). Large volcanic eruptions are mostly sourced above mobile basal mantle structures. *Communications Earth & Environment*, *6*(1), 538. https://doi.org/10.1038/s43247-025-02482-z
10. Doucet, L. S., Li, Z.-X., Ernst, R. E., Kirscher, U., El Dien, H. G., & Mitchell, R. N. (2020). Coupled supercontinent–mantle plume events evidenced by oceanic plume record. *Geology*, *48*(2), 159-163. https://doi.org/10.1130/G46754.1
11. Ernst, R. E. (2014). *Large igneous provinces*. Cambridge University Press. https://doi.org/10.1017/CBO9781139025300
12. Ernst, R. E., & Youbi, N. (2017). How Large Igneous Provinces affect global climate, sometimes cause mass extinctions, and represent natural markers in the geological record. *Palaeogeography, palaeoclimatology, palaeoecology*, *478*, 30-52. https://doi.org/10.1016/j.palaeo.2017.03.014
13. Flament, N., Bodur, O. F., Williams, S. E., & Merdith, A. S. (2022). Assembly of the basal mantle structure beneath Africa. *Nature*, *603*(7903), 846-851. https://doi.org/10.1038/s41586-022-04538-y

14. Flament, N., Gurnis, M., Müller, R. D., Bower, D. J., & Husson, L. (2015). Influence of subduction history on South American topography. *Earth and Planetary Science Letters*, *430*, 9-18. https://doi.org/10.1016/j.epsl.2015.08.006
15. Flament, N., Gurnis, M., Williams, S., Seton, M., Skogseid, J., Heine, C., & Müller, R. D. (2014). Topographic asymmetry of the South Atlantic from global models of mantle flow and lithospheric stretching. *Earth and Planetary Science Letters*, *387*, 107-119. https://doi.org/10.1016/j.epsl.2013.11.017
16. Frasson, T., Labrosse, S., Nataf, H.-C., Coltice, N., & Flament, N. (2024). On the impact of true polar wander on heat flux patterns at the core–mantle boundary. *Solid Earth*, *15*(5), 617-637. https://doi.org/10.5194/se-15-617-2024
17. French, S., & Romanowicz, B. A. (2014). Whole-mantle radially anisotropic shear velocity structure from spectral-element waveform tomography. *Geophysical Journal International*, *199*(3), 1303-1327. https://doi.org/10.1093/gji/ggu334
18. Gomi, H., Ohta, K., Hirose, K., Labrosse, S., Caracas, R., Verstraete, M. J., & Hernlund, J. W. (2013). The high conductivity of iron and thermal evolution of the Earth's core. *Physics of the Earth and Planetary Interiors*, *224*, 88-103. https://doi.org/10.1016/j.pepi.2013.07.010
19. Grove, T. L., & Parman, S. W. (2004). Thermal evolution of the Earth as recorded by komatiites. *Earth and Planetary Science Letters*, *219*(3-4), 173-187. https://doi.org/10.1016/S0012-821X(04)00002-0
20. Gubbins, D., Alfe, D., Masters, G., Price, G. D., & Gillan, M. (2003). Can the Earth's dynamo run on heat alone? *Geophysical Journal International*, *155*(2), 609-622. https://doi.org/10.1046/j.1365-246X.2003.02064.x
21. Hassan, R., Flament, N., Gurnis, M., Bower, D. J., & Müller, D. (2015). Provenance of plumes in global convection models. *Geochemistry, Geophysics, Geosystems*, *16*(5), 1465-1489. https://doi.org/10.1002/2015GC005751

22. Hernlund, J. W., & Houser, C. (2008). On the statistical distribution of seismic velocities in Earth's deep mantle. *Earth and Planetary Science Letters*, 265(3-4), 423-437. https://doi.org/10.1016/j.epsl.2007.10.042

23. Heyn, B. H., Conrad, C. P., & Trønnes, R. G. (2020). How thermochemical piles can (periodically) generate plumes at their edges. *Journal of Geophysical Research: Solid Earth*, *125*(6), e2019JB018726. https://doi.org/10.1029/2019JB018726

24. Houser, C., Masters, G., Shearer, P., & Laske, G. (2008). Shear and compressional velocity models of the mantle from cluster analysis of long-period waveforms. *Geophysical Journal International*, *174*(1), 195-212. https://doi.org/10.1111/j.1365-246X.2008.03763.x

25. Jaupart, C., Labrosse, S., Lucazeau, F., & Mareschal, J. (2007). 7.06-temperatures, heat and energy in the mantle of the earth. *Treatise on Geophysics*, *7*, 223-270. https://doi.org/10.1016/B978-0-444-53802-4.00126-3

26. Johansson, L., Zahirovic, S., & Müller, R. D. (2018). The interplay between the eruption and weathering of large igneous provinces and the deep-time carbon cycle. *Geophysical Research Letters*, *45*(11), 5380-5389. https://doi.org/10.1029/2017GL076691

27. Korenaga, J. (2006). Archean geodynamics and the thermal evolution of Earth. *Geophysical Monograph-American Geophysical Union*, *164*, 7. https://doi.org/10.1029/164GM03

28. Korenaga, J. (2007). Thermal cracking and the deep hydration of oceanic lithosphere: A key to the generation of plate tectonics? *Journal of Geophysical Research: Solid Earth*, *112*(B5). https://doi.org/10.1029/2006JB004502

29. Korenaga, J. (2008). Urey ratio and the structure and evolution of Earth's mantle. *Reviews of Geophysics*, *46*(2). https://doi.org/10.1029/2007RG000241

30. Korenaga, J. (2017). Pitfalls in modeling mantle convection with internal heat production. *Journal of Geophysical Research-Solid Earth*, *122*(5), 4064-4085. https://doi.org/10.1002/2016jb013850

31. Kustowski, B., Ekström, G., & Dziewoński, A. (2008). Anisotropic shear-wave velocity structure of the Earth's mantle: A global model. *Journal of Geophysical Research: Solid Earth*, *113*(B6). https://doi.org/10.1029/2007JB005169
32. Labrosse, S. (2002). Hotspots, mantle plumes and core heat loss. *Earth and Planetary Science Letters*, *199*(1-2), 147-156. https://doi.org/10.1016/S0012-821X(02)00537-X
33. Labrosse, S. (2015). Thermal evolution of the core with a high thermal conductivity. *Physics of the Earth and Planetary Interiors*, *247*, 36-55. https://doi.org/10.1016/j.pepi.2015.02.002
34. Labrosse, S., & Jaupart, C. (2007). Thermal evolution of the Earth: Secular changes and fluctuations of plate characteristics. *Earth and Planetary Science Letters*, *260*(3-4), 465-481. https://doi.org/10.1016/j.epsl.2007.05.046
35. Lay, T., Hernlund, J., & Buffett, B. A. (2008). Core–mantle boundary heat flow. *Nature Geoscience*, *1*(1), 25-32. https://doi.org/10.1038/ngeo.2007.44
36. Li, M., Puetz, S., Condie, K., & Olson, P. (2023). Mantle plume heat flux and surface motion periodicities and their implications for the growth of continental crust. *Earth and Planetary Science Letters*, *611*, 118148. https://doi.org/10.1016/j.epsl.2023.118148
37. Li, M., Zhong, S., & Olson, P. (2018). Linking lowermost mantle structure, core-mantle boundary heat flux and mantle plume formation. *Physics of the Earth and Planetary Interiors*, *277*, 10-29. https://doi.org/10.1016/j.pepi.2018.01.010
38. Li, Y., Deschamps, F., & Tackley, P. J. (2014). Effects of low-viscosity post-perovskite on the stability and structure of primordial reservoirs in the lower mantle. *Geophysical Research Letters*, *41*(20), 7089-7097. https://doi.org/10.1002/2014GL061362
39. Lomb, N. R. (1976). Least-squares frequency analysis of unequally spaced data. Astrophysics and space science, 39(2), 447-462. https://doi.org/10.1007/BF00648343
40. MacQueen, J. (1967). Multivariate observations. Proceedings ofthe 5th Berkeley Symposium on Mathematical Statisticsand Probability,

41. McNamara, A. K., & Zhong, S. (2004). The influence of thermochemical convection on the fixity of mantle plumes. *Earth and Planetary Science Letters*, *222*(2), 485-500. https://doi.org/10.1016/j.epsl.2004.03.008

42. Müller, R. D., Flament, N., Cannon, J., Tetley, M. G., Williams, S. E., Cao, X., Bodur, Ö. F., Zahirovic, S., & Merdith, A. (2022). A tectonic-rules-based mantle reference frame since 1 billion years ago – implications for supercontinent cycles and plate–mantle system evolution. *Solid Earth*, *13*(7), 1127-1159. https://doi.org/10.5194/se-13-1127-2022

43. Nakagawa, T. (2020). A coupled core-mantle evolution: review and future prospects. *Progress in Earth and Planetary Science*, *7*(1). https://doi.org/10.1186/s40645-020-00374-8

44. Nakagawa, T., & Tackley, P. J. (2004). Effects of thermo-chemical mantle convection on the thermal evolution of the Earth's core. *Earth and Planetary Science Letters*, *220*(1-2), 107-119. https://doi.org/10.1016/S0012-821x(04)00055-X

45. Nakagawa, T., & Tackley, P. J. (2008). Lateral variations in CMB heat flux and deep mantle seismic velocity caused by a thermal–chemical-phase boundary layer in 3D spherical convection. *Earth and Planetary Science Letters*, *271*(1-4), 348-358. https://doi.org/10.1016/j.epsl.2008.04.013

46. Nakagawa, T., & Tackley, P. J. (2012). Influence of magmatism on mantle cooling, surface heat flow and Urey ratio. *Earth and Planetary Science Letters*, *329*, 1-10. https://doi.org/10.1016/j.epsl.2012.02.011

47. Nimmo, F. (2015). Energetics of the core. *Treatise on Geophysics*, *8*, 27-55. https://doi.org/10.1016/B978-044452748-6.00128-0

48. Nisbet, E. G., & Fowler, C. M. R. (1983). Model for Archean plate tectonics. *Geology*, *11*(7), 376-379. https://doi.org/10.1130/0091-7613(1983)11<376:MFAPT>2.0.CO;2

49. O'Malley, C. P., Roberts, G. G., Panton, J., Richards, F. D., Davies, J. H., Fernandes, V. M., & Ghelichkhan, S. (2024). Reconciling surface deflections from simulations of global mantle

convection. *Geoscientific Model Development*, *17*(24), 9023-9049. https://doi.org/10.5194/gmd-17-9023-2024

50. Olson, P. (2016). Mantle control of the geodynamo: Consequences of top-down regulation. *Geochemistry, Geophysics, Geosystems*, *17*(5), 1935-1956. https://doi.org/10.1002/2016GC006334
51. Olson, P., & Amit, H. (2015). Mantle superplumes induce geomagnetic superchrons. *Frontiers in Earth Science*, *3*, 38. https://doi.org/10.3389/feart.2015.00038
52. Prokoph, A., El Bilali, H., & Ernst, R. (2013). Periodicities in the emplacement of large igneous provinces through the Phanerozoic: Relations to ocean chemistry and marine biodiversity evolution. *Geoscience Frontiers*, *4*(3), 263-276. https://doi.org/10.1016/j.gsf.2012.08.001
53. Richards, M. A., Duncan, R. A., & Courtillot, V. E. (1989). Flood basalts and hot-spot tracks: plume heads and tails. *Science*, *246*(4926), 103-107. https://doi.org/10.1126/science.246.4926.103
54. Ritsema, J., Deuss, A., Van Heijst, H., & Woodhouse, J. (2011). S40RTS: a degree-40 shear-velocity model for the mantle from new Rayleigh wave dispersion, teleseismic traveltime and normal-mode splitting function measurements. *Geophysical Journal International*, *184*(3), 1223-1236. https://doi.org/10.1111/j.1365-246X.2010.04884.x
55. Savitzky, A., & Golay, M. J. (1964). Smoothing and differentiation of data by simplified least squares procedures. Analytical chemistry, 36(8), 1627-1639. https://doi.org/10.1021/ac60214a047
56. Scargle, J. D. (1982). Studies in astronomical time series analysis. II-Statistical aspects of spectral analysis of unevenly spaced data. Astrophysical Journal, Part 1, vol. 263, Dec. 15, 1982, p. 835-853., 263, 835-853. https://doi.org/10.1086/160554

57. Sharpe, H. N., & Peltier, W. (1979). A thermal history model for the Earth with parameterized convection. *Geophysical Journal International*, *59*(1), 171-203. https://doi.org/10.1111/j.1365-246X.1979.tb02560.x
58. Simmons, N. A., Forte, A. M., Boschi, L., & Grand, S. P. (2010). GyPSuM: A joint tomographic model of mantle density and seismic wave speeds. *Journal of Geophysical Research: Solid Earth*, *115*(B12). https://doi.org/10.1029/2010JB007631
59. Tan, E., Leng, W., Zhong, S., & Gurnis, M. (2011). On the location of plumes and lateral movement of thermochemical structures with high bulk modulus in the 3-D compressible mantle. *Geochemistry, Geophysics, Geosystems*, *12*(7). https://doi.org/10.1029/2011GC003665
60. Tappe, S., Smart, K., Torsvik, T., Massuyeau, M., & de Wit, M. (2018). Geodynamics of kimberlites on a cooling Earth: Clues to plate tectonic evolution and deep volatile cycles. *Earth and Planetary Science Letters*, *484*, 1-14. https://doi.org/10.1016/j.epsl.2017.12.013
61. Zhong, S. (2006). Constraints on thermochemical convection of the mantle from plume heat flux, plume excess temperature, and upper mantle temperature. *Journal of Geophysical Research: Solid Earth*, *111*(B4). https://doi.org/10.1029/2005JB003972
62. Zhong, S., McNamara, A., Tan, E., Moresi, L., & Gurnis, M. (2008). A benchmark study on mantle convection in a 3-D spherical shell using CitcomS. *Geochemistry, Geophysics, Geosystems*, *9*(10). https://doi.org/10.1029/2008gc002048

Supplementary materials

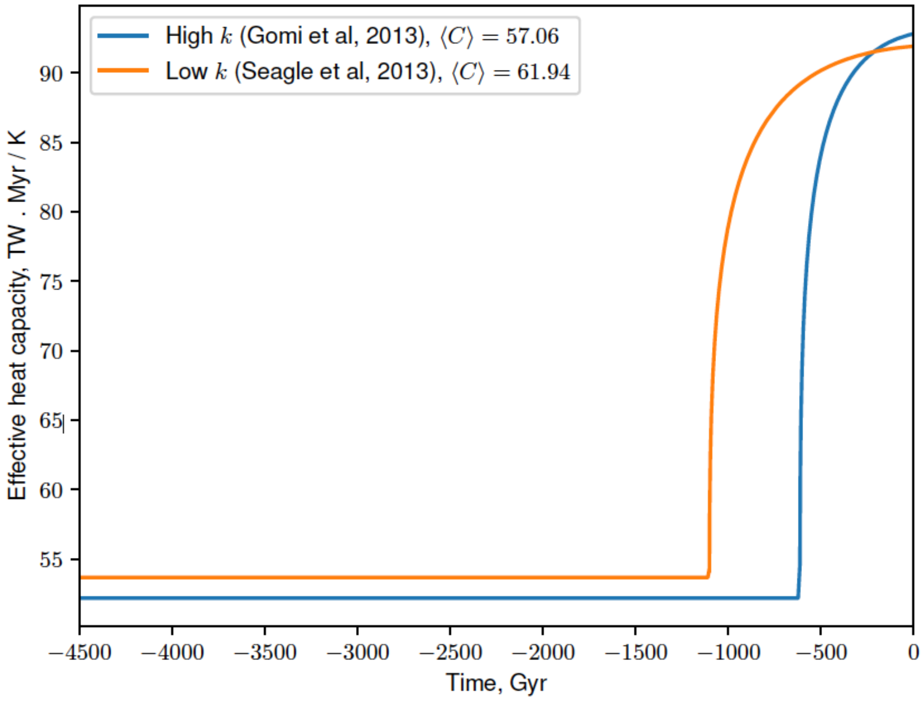

Figure S1. Evolution of the effective total heat capacity of Earth's core. The orange line shows the result from Seagle et al. (2013), and the blue line shows the result from Gomi et al. (2013), where the thermal conductivity was enhanced.

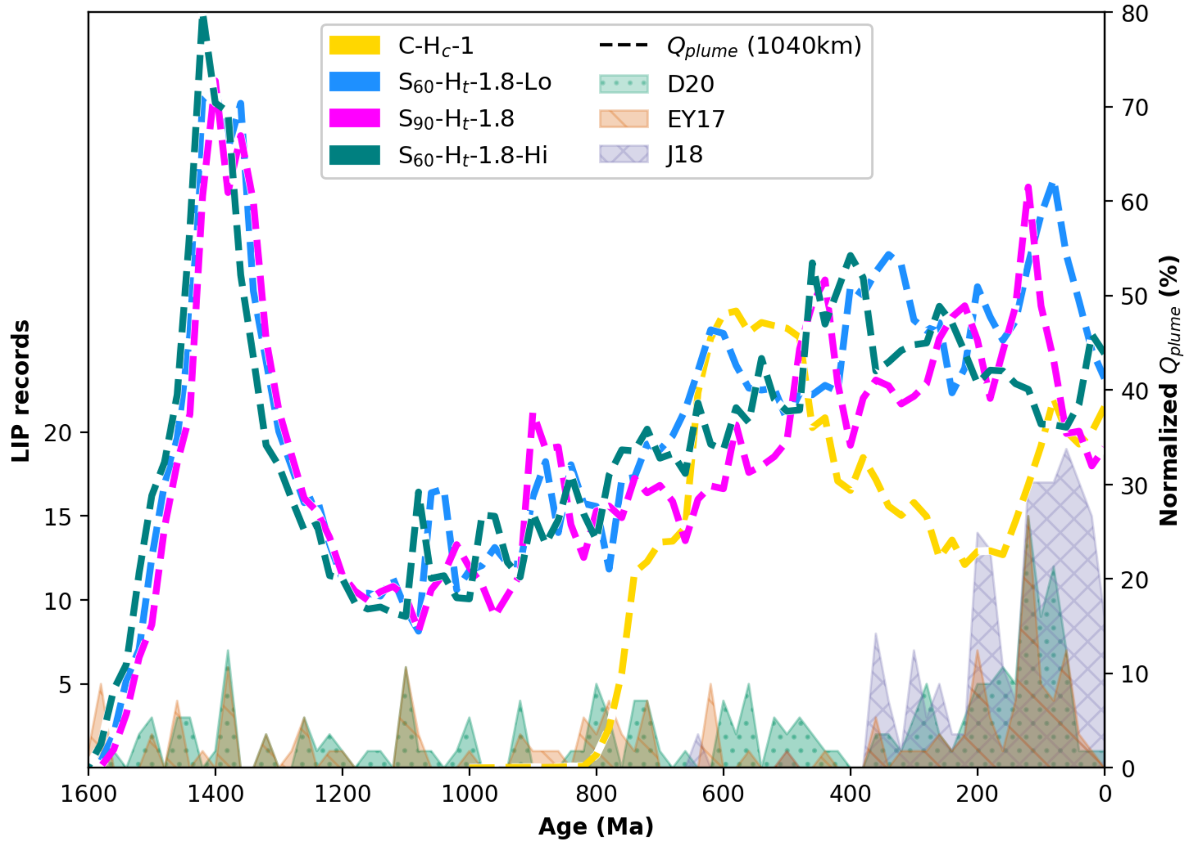

Figure S2. Evolution of plume heat flux for all models, compared with three sets of LIP records ('D20': Doucet et al., 2020; ' EY17': Ernst and Youbi, 2017; 'J18': Johansson et al., 2018). The dotted lines denote the heat flux carried by plumes for different cases (in different colours). The shaded areas in different patterns and colours represent LIP records from different LIP databases.

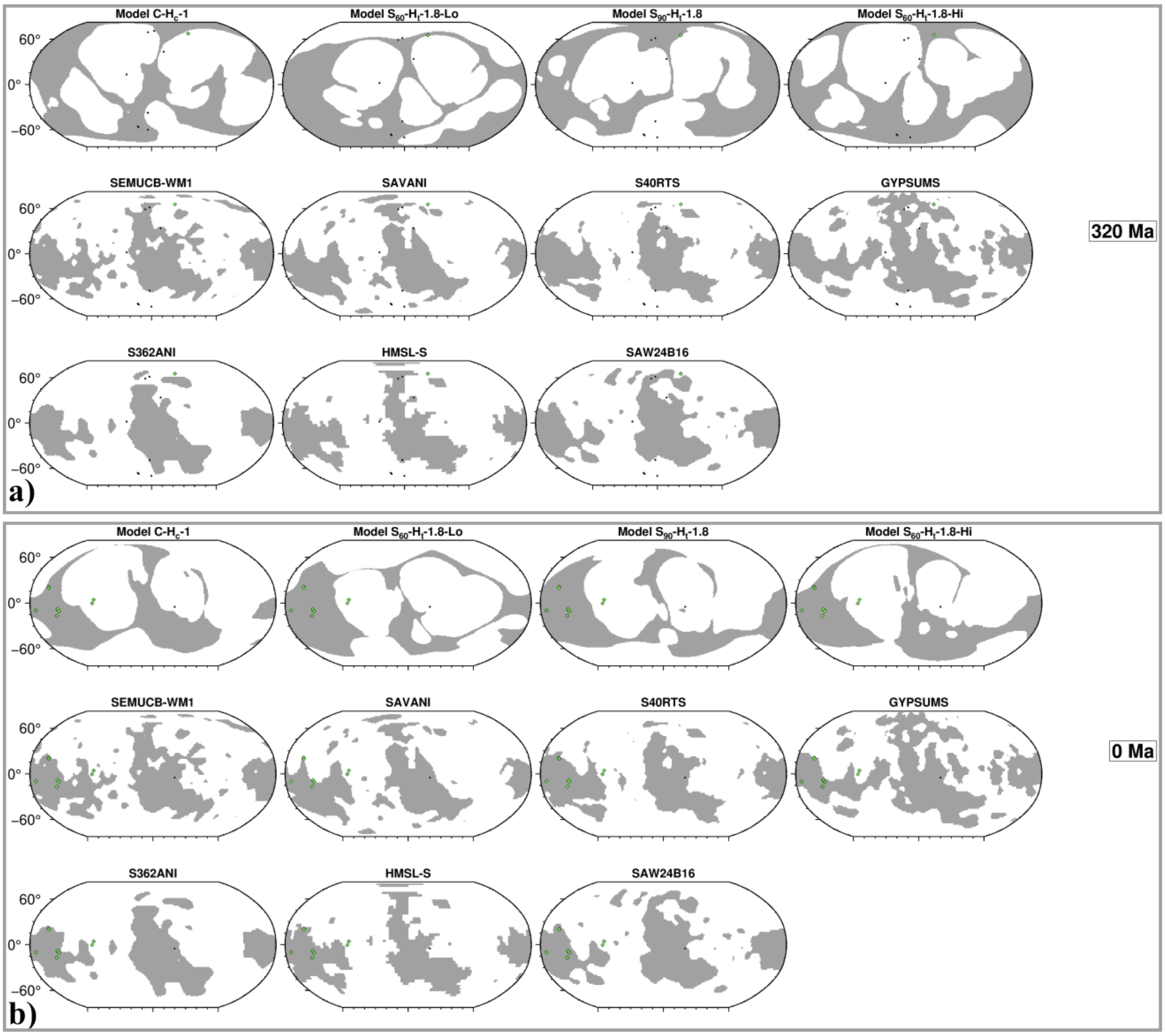

Figure S3. Model cluster maps (1000-2800 km depth), seismic tomographic model cluster maps, and volcanic eruptions at 320 Ma (**a**) and present-day (**b**). The grey regions denote BLOBS. The green diamonds and black dots represent reconstructed LIP locations from Johansson et al. (2018) and kimberlite locations from Tappe et al. (2018).

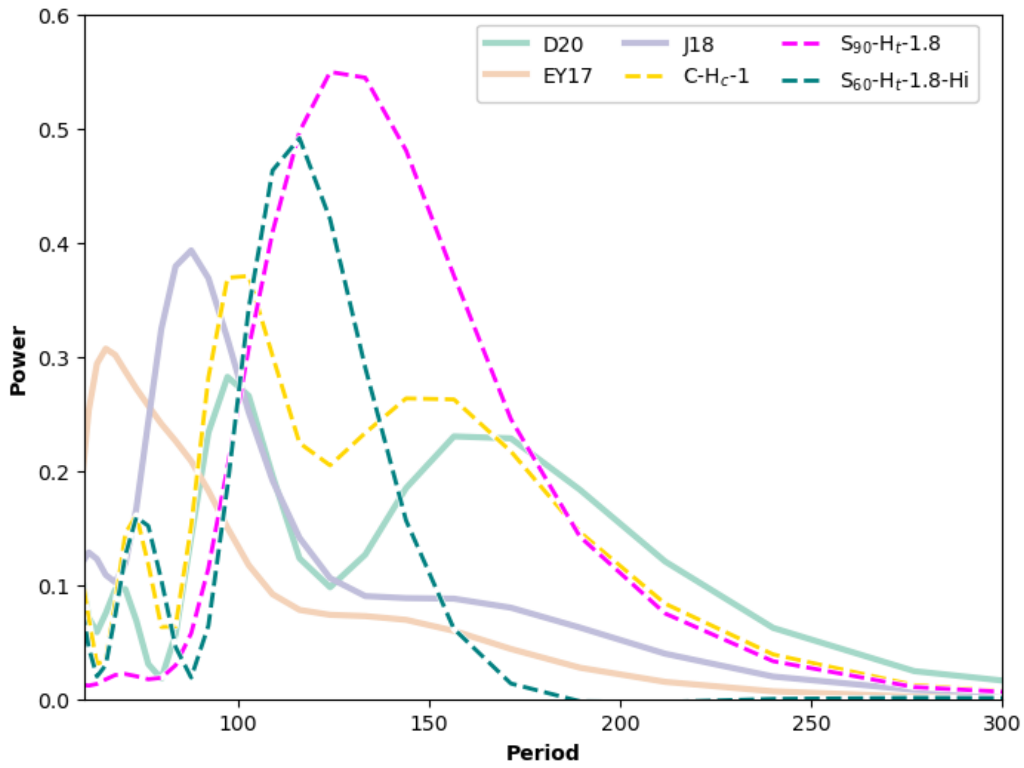

Figure S4. Periodograms for models C-H$_c$-1, S$_{90}$-H$_t$-1.8, and S$_{60}$-H$_t$-1.8-Hi from 360 Ma to the present day (dashed lines), and for all three LIP databases (D20, EY17, and J18) from 320 Ma to the present day (solid lines). Only periods ≥ 60 Myr are presented. Colours represent different models/LIP databases and are consistent with those in Fig. 8a.

Table S1. Radiogenic heat production.

Isotope	h_n	λ_n(1/Gyr)
^{238}U	0.372	0.155
^{235}U	0.0164	0.985
^{232}Th	0.43	0.0495
^{40}K	0.181	0.555

Table S2. Initial ΔT across the considered models.

Model	**Initial ΔT (K)**
C-H_c-1	3103
S_{60}-H_t-1.8-Lo	3503
S_{90}-H_t-1.8	3338
S_{60}-H_t-1.8-Hi	3761